nature communications

Article

https://doi.org/10.1038/s41467-026-72813-x

Ultrafast laser induces macroscopic symmetry-breaking of diamond color centers

Received: 3 June 2025

Accepted: 23 April 2026

Published online: 12 May 2026

Check for updates

Yang Gao[1], Qi-Zheng Ji[1], Chao-Bo Liu[1], Qi Xiao[1] & Chao Lian[2,3]

The negatively charged nitrogen-vacancy center is a leading quantum platform due to its excellent spin coherence and stable interactions. Understanding its ultrafast dynamics is crucial for quantum applications but presents significant challenges for both experimental characterization and atomic-scale modeling. Here, we employ real-time time-dependent density functional theory to investigate the coupled electron-phonon-spin dynamics in negatively charged nitrogen-vacancy centers. Laser excitation promotes minority-spin electrons within 100 fs, establishing a C_{3v}-symmetry breaking charge ordering. Subsequently, ionic motion on the potential energy surface of the excited electrons generates both symmetric oscillations of carbon-nitrogen bonds and dynamic Jahn-Teller distortions with a C_{3v}-symmetry breaking. These distortions subsequently induce nonlocal coherent phonons in the diamond lattice, which propagate with the C_{3v}-symmetry breaking at the sound velocity (~ 2 Å/fs). Our simulations provide direct time-resolved visualization of these processes, offering novel insights into the microscopic interplay of electrons, phonons, and spins in nitrogen-vacancy centers.

The negatively charged nitrogen-vacancy (NV^-) center has become a leading platform in quantum sensing, networking, and computation[1–4], due to its exceptional spin coherence time, distinct opto-magnetic and electron-phonon interactions, and remarkable stability over a wide temperature range[5]. In these applications, the intricate coupling between light, electronic spin, and phonons, particularly the role of local vibrational modes (LVMs, Fig. 1a) are crucial in modulating optical properties[4,6,7], while these interactions are entangled in the ground state or weakly perturbed state and thus difficult to understand and manipulate individually.

Pump-probe experiments have revolutionized the study by categorizing the mixed electron-phonon-spin correlations into different timescales in non-equilibrium ultrafast dynamics[8–13]. Pioneering work by Huxter et al. utilized two-dimensional ultrafast spectroscopy to reveal the dominant role of LVMs in mediating vibrational bath responses[8]. Particularly, the dynamical Jahn-Teller (DJT) distortion has been established as the primary mechanism driving femtosecond-scale depolarization of NV^- electronic states[9]. Recent advances by Carbery et al. distinguished the timescales of DJT decay (~ 150 fs) and excited-state relaxation (picosecond-scale)[13], while Ichikawa et al. demonstrated that a special LVM, dynamical polarons, serve as precursors to long-lived nonlocal coherent phonons (NLCP)[14]. These results collectively highlight the critical role of phonons in NV^- center dynamics from different aspects.

A comprehensive atomic-scale understanding of ultrafast processes in NV^- centers is crucial for reconciling these macroscopic spectroscopy into a unified framework. For the ground-state NV^- systems, first-principles methodologies have proven instrumental in systematically probing couplings between light and electrons[15–18], electrons and phonons[11,19–21], and phonons and spins[22–25]. However, modeling non-equilibrium dynamics presents formidable computational challenges: ab initio simulations must concurrently resolve spin-

[1]Beijing Institute of Spacecraft Environment Engineering, Beijing, PR China. [2]Beijing National Laboratory for Condensed Matter Physics and Institute of Physics, Chinese Academy of Sciences, Beijing, PR China. [3]Songshan Lake Materials Laboratory, Dongguan City, Guangdong Province, PR China.
e-mail: chaolian@iphy.ac.cn

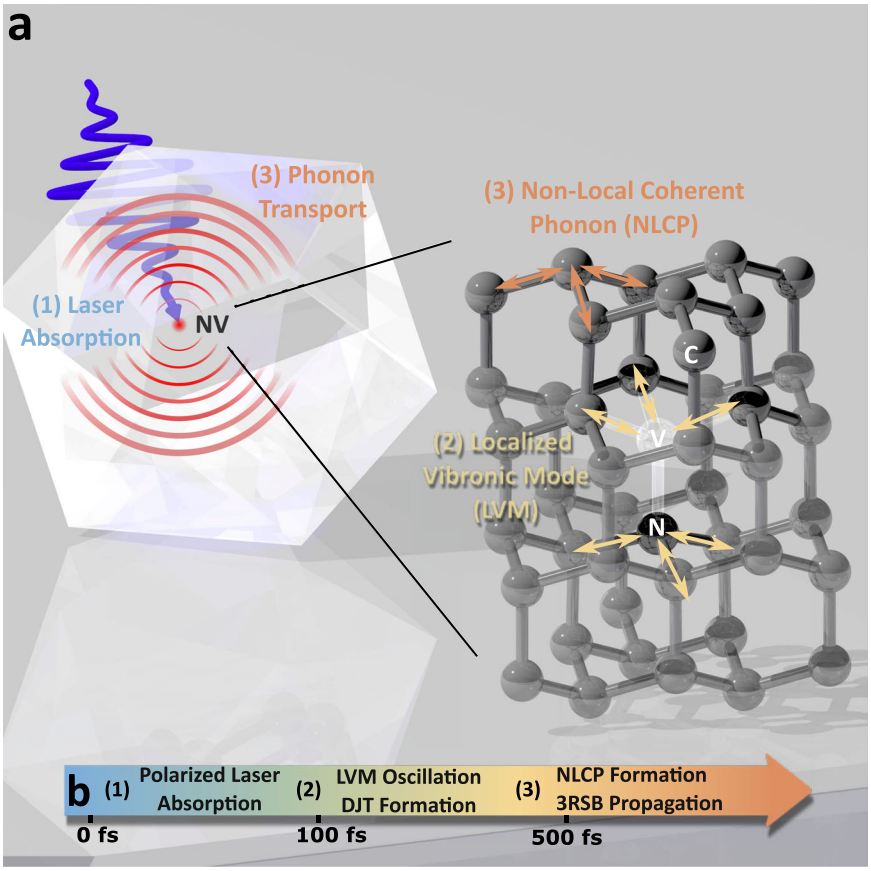

Fig. 1 | Schematic diagrams of laser-excited NV^- centers. a The overall laser-induced dynamics in NV^- centers: (1) laser excitation of electrons, (2) induction of local vibrational mode (LVM) vibrations near the NV^- centers, and subsequently (3) excitation of nonlocal coherent phonons (NLCP) modes via phonon propagation. **b** Corresponding ultrafast timescales of the processes described in **a**.

orbit-mediated light-electron-phonon-spin interactions, while bridging the six orders of magnitude difference between attosecond electronic time steps and picosecond phonon dynamics.

Our recent methodological advancements[26–28] of the real-time time-dependent density functional theory (RT-TDDFT)[29,30] overcome these limitations through optimized wavefunction propagation schemes that integrate three key components: explicit spin-orbit coupling (SOC) in time-dependent Hamiltonians[31], velocity-gauge treatment of electromagnetic fields[32], and excited-state molecular dynamics capabilities. By applying this advanced RT-TDDFT framework to NV^- center systems, we aim to unravel the real-time interplay of electronic, vibrational, and spin degrees of freedom, thereby establishing a new dynamical paradigm for quantum defect research. With the unique atomic-level picture obtained with TDDFT, we propose that the ultrafast combined symmetric oscillations of carbon-nitrogen bonds and DJT distortions propagate through the diamond crystal with the speed of sound and generate a macroscopic coherent symmetry-breaking.

Results and discussion

Photocarrier generation

Under a linearly polarized laser pulse with 100 fs duration, we first analyze the electronic excitation in the NV^- center system. The total photoinduced carrier density is quantified as

$$n_{pc}(t) = \sum_{n\mathbf{k}} |f_{n\mathbf{k}}(t) - f_{n\mathbf{k}}(0)|, \quad (1)$$

where $f_{n\mathbf{k}}$ represents the time-dependent electronic population at band n and crystal momentum $\mathbf{k}$. During the laser pulse, approximately $n_{pc} = 0.15$ carriers are generated [Fig. 2a]. The transient energy per carrier is calculated as $E_{ave}(t) = [E_{KS}(t) - E_{KS}(0)]/n_{pc}$, where $E_{KS}(t)$ denotes the time-dependent Kohn-Sham energy[29]. As shown in the inset of Fig. 2a, E_{ave} reaches ~ 2.2 eV/carrier at $t = 100$ fs, consistent with the incident photon energy of 1.945 eV with energy broadening 0.3 eV. This indicates that the first-order photon absorption dominating at this laser intensity, which is consistent with the experimental setups[8,9,13,14].

The photoinduced charge density redistribution is shown in Fig. 2b. The spatial asymmetry reveals a p_z-orbital-shaped wavefunction localized at the nitrogen (N) atom and three p_x/p_y-orbital-like lobes near the vacancy (V) site. This is consistent with the transition from the $a\downarrow$ state to the $e\downarrow$ manifold as shown in Fig. 2e and f. Notably, the p_x/p_y-like charge distributions exhibit a C_{3v}-symmetry breaking (3RSB): the lobe perpendicular to the laser polarization direction (E) is suppressed, while the two lobes along the C_3 and C_3^2 symmetry axes remain equivalent. For $t > 100$ fs, the electron-electron scattering processes promote electrons from the $e\uparrow$ states into the conduction bands of bulk diamond.

The spin polarization remains almost unchanged during the subsequent electron-phonon dynamics, as shown in Fig. 2(d). This agrees well with previous studies that the perpendicular component of the SOC ($\lambda_\perp$), which is responsible for spin flipping, is considered negligible in the ^3E triplet[33,34]. This observed spin stability enables the efficient laser initialization of the electronic spin into the $m_s = 0$ ground state[1]. These results reproduce the well-established excitation pathways[1,6,13] and establishes a rigorous foundation for simulating subsequent coupled electron-phonon processes with full quantum-mechanical fidelity.

https://doi.org/10.1038/s41467-026-72813-x

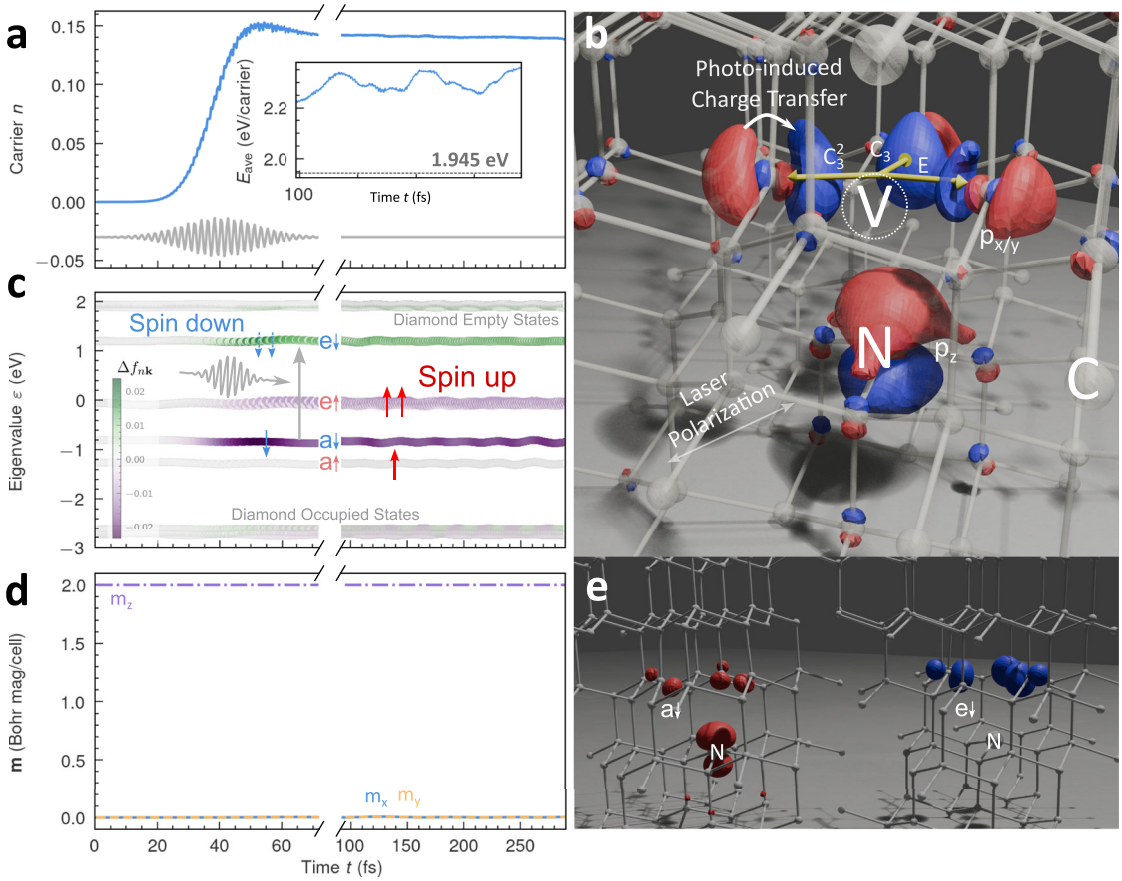

Fig. 2 | Electronic, and spin dynamics in the NV⁻ system. a Number of excited carrier as a function of time. Gray curve: Laser electric field component. Inset: Time-dependent average energy per carrier (E_{ave}). **b** Differential electronic density between $t = 100$ fs and $t = 0$, showing charge redistribution (blue: positive $\Delta\rho$; red: negative $\Delta\rho$). **c** Time-resolved eigenvalue evolution near Fermi energy ($\mathbf{k} = \Gamma$), with color scale ($\Delta f_{n\mathbf{k}}$) indicating electronic population changes. **d** Evaluation of m_x, m_y, and m_z as the function of time. **e**–**f** the wavefunctions of the $a\downarrow$ orbitals and $e\downarrow$ orbitals, respectively. Isosurface level is 5×10^{-4} e/Å^3.

LVMs and spin dynamics

On longer timescales > 100 fs, the electron-phonon-spin system exhibits strongly coupled dynamical behavior. First we analyze the LVM dynamics by monitoring the triangle formed by the three carbon atoms around the V site, with lengths d_1, d_2, and d_3, as shown in the left inset of Fig. 3a. The average bond length $d = (d_1 + d_2 + d_3)/\sqrt{3}$, is used to describe the symmetric A_1 mode and the degenerate E representation is formed by the combinations $\delta d_x = (d_1 + d_2 - 2d_3)/\sqrt{6}$, $\delta d_y = (d_1 - d_2)/\sqrt{2}$. $d(t)$ oscillations [Fig. 3a] with amplitudes of ~ 0.02 Å show striking agreement with experimental two-dimensional ultrafast spectra[8] in both time and frequency domains, confirming that the LVMs directly modulate the optical properties of NV⁻ centers.

More importantly, δd_x exhibits an oscillation about 1×10^{-3} Å [Fig. 3c], which is the microscopic characteristic of DJT distortion[35]. In comparison, when the laser polarization is aligned parallel to the NV center axis [left inset of Fig. 3a], the 3RSB is eliminated while the oscillations of LVMs remain qualitatively similar, as shown in Fig. 3a and c. This indicates that the DJT distortion is a direct result of 3RSB charge transfer. The photo-induced charge transfer is weaker along the **E**-axis compared to that along C_3 and C_3^2 directions (Fig. 2b), which causes a 3RSB in the photo-induced ion forces. The peaks in the Fourier transform of Δd_y spectrum, shown in the inset of Fig. 3c, are consistent with the E symmetry vibronic levels reported in Ref. 35, providing another characteristic fingerprint for comparison with Δ-SCF calculations[35].

We analyze the bond dynamics with the potential energy surface (PES) by analyze the $E_{KS}(t)$ along these two coordinates d and δd_x, i.e., $E_{KS}(d)$ and $E_{KS}(\delta d_x)$.$E_{tot}(d)$ shows a parabolic PES with a minimum at the excited-state equilibrium bond length (Fig. 3b), corresponding to overall oscillations, while $E_{tot}(\delta d_x)$ reveals a double-well PES (Fig. 3d) characteristic of the DJT distortion.

This PES evolution has great influence on the structural response, similar to the PES modification predicted[28] and the non-linear pump-probe signal observed in $TiSe_2$[36]. This directly resolve these competing effects with a critical advance over previous excited-state PES studies relying on perturbative methods like ΔSCF[35].

Phonon propagation

Beyond local symmetry breaking, the DJT distortion induces macroscopic NLCPs with 3RSB in diamond. We analyze the oscillation amplitudes $\Delta\tau_i(t) = \boldsymbol{\tau}_i(t) - \boldsymbol{\tau}_i(0)$ of the C atoms in successive coordination shells (1-4) around the V site (Fig. 4a), where $\tau_i(t)$ is the position of the i-th C atom. Figure 4b shows that during 0-50 fs, $\Delta\tau_i(t)$ values are degenerate for all three C atoms in each shell, while over a longer period (50-150 fs), the atoms along the C_3 and C_3^2 directions retain degenerate amplitudes, and the atom along the **E**-axis exhibits a reduced amplitude, indicating the emergence of 3RSB in NLCPs besides the LVMs.

This 3RSB NLCPs propagates radially, evidenced by a delayed onset and reduced amplitudes in outer shells. The 40 fs delay between the NV⁻ center and shell 4 agree well with the 50 fs NLCP formation time proposed in ref. 14. Quantifying displacements via the maximum amplitude $\max\{\Delta\tau_i(t_f)\}$ for $t < t_f$ (Fig. 4c), we find that only LVMs are excited at $t = 35$ fs, while oscillation amplitudes saturate for C atoms in

https://doi.org/10.1038/s41467-026-72813-x

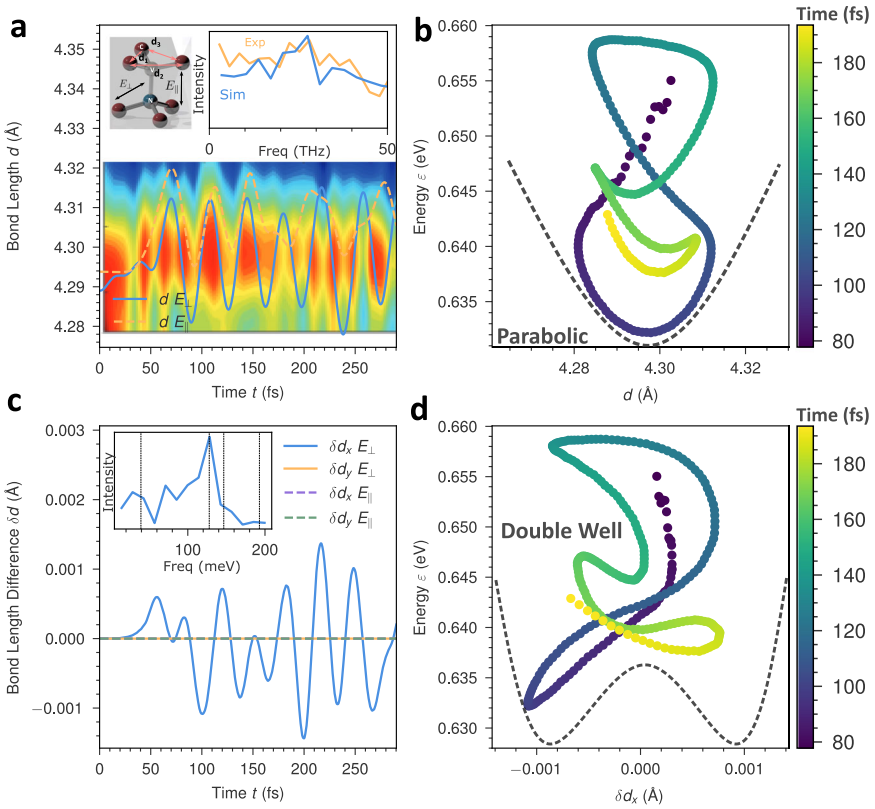

Fig. 3 | Dynamics of the local vibrational mode. a Average bond length $d = (d_1 + d_2 + d_3)/\sqrt{3}$ as a function of time, where d_i ($i = 1, 2, 3$) are the lengths of the bonds between the nearest carbon atoms and the vacancy (V) site, as illustrated in Inset (left). The solid line represents the result for laser polarization perpendicular to the NV axis ($E_\perp$), and the dashed line for polarization parallel to the NV axis ($E_\parallel$), as defined in Inset (left). The contour plot is generated using data from Fig. 2f of ref. 8. Inset (right) shows the Fourier transform of $d(t)$ compared with experimental data from ref. 8. **b** Dynamical potential energy surface (PES) as a function of bond length d. For comparison, a parabolic PES is indicated by a dashed line. Colors represent different times. **c** Differences in bond lengths δd_y and δd_x as a function of time. Solid and dashed lines denote results for $E_\perp$ and $E_\parallel$, respectively. Inset shows the Fourier transform of $\delta d_x(t)$ compared with the vibrational frequencies reported in ref. 35. **d** Dynamical PES as a function of the bond-length difference δd_x. A double-well PES is shown as a dashed line for comparison. Colors represent different times.

shells 1-3 at $t = 100$ fs. The average maximum amplitude over the whole cell at different t_f (Fig. 4d) is evaluated as

$$\overline{\max\{\Delta\tau_i(t_f)\}} = \frac{1}{N_{\text{atom}}}\sum_{i=1}^{N_{\text{atom}}} \max\{\Delta\tau_i(t_f)\}, \tag{2}$$

where N_{atom} is the total number of atoms in the calculated region. We found that the $\overline{\max\{\Delta\tau_i(t_f)\}}$ can be well described with a diffusion-like relation:

$$\overline{\max\{\Delta\tau_i(t_f)\}} = A\exp\left(-\frac{1}{4Dt_f}\right) + C, \tag{3}$$

with A = 0.20 Å, C = -0.19 Å, and D = 0.25 Å/fs. The diffusion speed D is close to the experimental sound velocity of diamond (0.19 Å/fs)[37], confirming the diffusion nature of the NLCP. Thus, we demonstrate that the DJT distortions trigger the macroscopic symmetry-breaking phonon transport.

The origin of the NLCP is the electric field generated by the excited-state electron distribution [Fig. 2]. We carry a calculation with six carbon atoms near the NV center fixed, i.e., the C1 atoms in Fig. 4a. As compared in Fig. 4b, it can be observed that not only is the onset of vibrations delayed for carbon atoms in different shells away from the NV center, but the vibrational amplitude also remains very small within the first 50 fs. Utilizing the previously described diffusion model (3) to characterize this propagation process, we obtain a new set of parameters with A = 0.25 Å, C = -0.24 Å, and D = 0.25 Å/fs. This indicates that diffusion mechanism is similar and the propagation speed remains the sound velocity of diamond.

Summary and discussion

In this work, we have elucidated the ultrafast coupled dynamics of electrons, phonons, and spins in the NV^- center following photoexcitation by leveraging RT-TDDFT. Our simulations directly capture a multi-stage dynamical sequence: Laser excitation initially promotes minority-spin electrons within 100 fs, establishing a charge-ordered state that breaks the C_{3v} symmetry. This electronic rearrangement subsequently drives ionic motion, generating both symmetric bond oscillations and DJT with 3RSB. These local distortions, in turn, launch NLCP wavepackets that propagate through the diamond lattice at the sound velocity, carrying the 3RSB signature.

The key finding of this study is the direct, time-resolved visualization of the process of the laser-induced 3RSB transfer, from the electronic excitation into specific lattice vibrations and propagation. These insights provide a novel fundamental understanding of the NV^- center's photophysics and suggest potential avenues for coherent control of its quantum state via tailored phononic environments, with implications for quantum information science.

Methods

Based on our previous efforts in developing the time-dependent ab initio package (TDAP)[28], alongside the velocity-gauge field algorithm[26,27] and molecular dynamics[27,38], we implemented the TDDFT algorithm[39] within the plane-wave code Quantum Espresso[40,41]. For

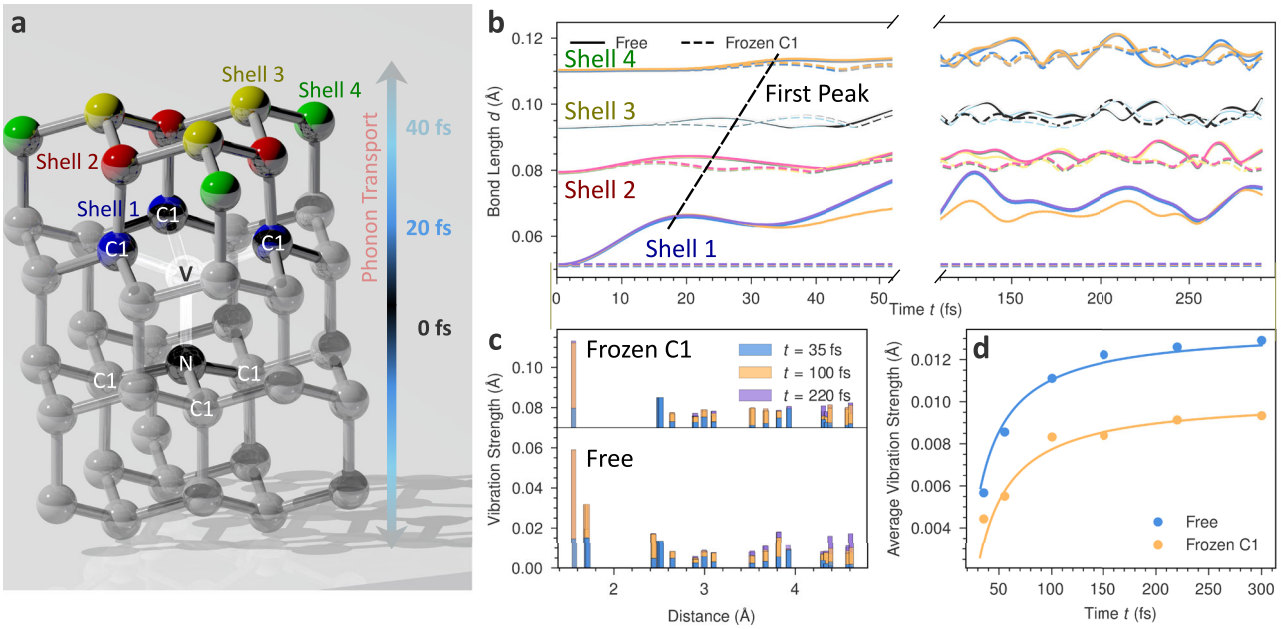

Fig. 4 | Macroscopic propagation of the C_{3v}-symmetry breaking. a Schematic of carbon atoms around the NV^- center in different shells and phonon transport. The atoms are categorized into different shells according to their distances to the vacancy (V) site and are marked in different colors. C1 atoms are those nearest to the NV^-. **b** Displacement $d(t)$ of carbon atoms in different shells as a function of time. The curve for each shell is shifted upward proportionally to its distance from the V site. The solid lines indicate the case with all atoms free, while the dashed lines indicate the case where C1 atoms are fixed. **c** Maximum displacement amplitude as a function of distance to the V site at different final times t_f (35, 100, and 400 fs). The upper panel shows results with C1 atoms fixed, and the lower panel shows results with all atoms free. **d** Average maximum displacement of carbon atoms as a function of t_f. Blue lines and symbols correspond to the case with all atoms free, and yellow lines and symbols correspond to the case with C1 atoms fixed.

details on the velocity-gauge electric field, the efficient evolution method, choice of the XC functionals, and the energy cutoff/ k-points convergence, please refer to the Supplementary Information of ref. 28. We used the Perdew-Burke-Ernzerhof (PBE) exchange-correlation (XC) functional[42] in both DFT and TDDFT calculations. The core electrons and nuclei were described using full-relativistic, optimized norm-conserving Vanderbilt pseudopotential (ONVP)[43] from the PseudoDojo pseudopotentials library[44]. The plane-wave energy cutoff was set to 80 Ry. The NV system is modeled as a 3 × 3 × 3 supercell of diamond with one NV center, containing 53 atoms (52 C atoms and 1 N atom). Brillouin zone was sampled using Monkhorst-Pack scheme[45] with a 3 × 3 × 3 k-point mesh. Band unfolding techniques were utilized to generate the effective band structures (EBS)[46,47] with unfold-x code[48]. The electron timestep δt is 4×10^{-4} a.u.=0.194 attosecond and the ion timestep Δt is 0.194 fs. Structural figures are generated with VESTA[49,50].

The Gaussian-type laser pulse is utilized

$$\mathbf{E}(t) = E_0 \hat{\mathbf{x}} \cos(\omega t) \exp\left[-\frac{(t-t_0)^2}{2\sigma^2}\right], \quad (4)$$

where E_0 = 0.03 V/Å is the peak field strength, ω = 1.945 eV is the laser frequency, t_0 = 40 fs is the Gaussian peak time, and σ = 12 fs is the Gaussian pulse width. We note here that the ω = 1.945 laser frequency used in the simulations does not physically correspond to the experimental ZPL excitation energy due to the well-known bandgap underestimation of the PBE functional. The choice of ω = 1.945 here is to be resonant with the calculated vertical excitation energy on the PBE energy scale. Please see the Supplementary Information for detailed discussion. $\hat{\mathbf{x}}$ denotes that the laser pulse is linearly polarized along the x direction. We have tested on different laser intensity E_0 from 0.01 V/Å to 0.06 V/Å and find that the results are similar with different amplitudes.

Data availability

The key data underpinning the conclusions of this work are included in the article. All raw data relevant to the findings of this study are available from the corresponding author (C.L.) upon request.

Code availability

Part of the computational codes that were used to generate the data is presented[51] and that the full code can be provided by the corresponding author (C.L.) upon request.

References

1. Barry, J. F. et al. Sensitivity optimization for NV-diamond magnetometry. *Rev. Mod. Phys.* **92**, 015004 (2020).
2. Wolfowicz, G. et al. Quantum guidelines for solid-state spin defects. *Nat. Rev. Mater.* **6**, 906 (2021).
3. Rovny, J. et al. Nanoscale diamond quantum sensors for many-body physics. *Nat. Rev. Phys.* **6**, 753 (2024).
4. Du, J., Shi, F., Kong, X., Jelezko, F. & Wrachtrup, J. Single-molecule scale magnetic resonance spectroscopy using quantum diamond sensors. *Rev. Mod. Phys.* **96**, 025001 (2024).
5. Degen, C. L., Reinhard, F. & Cappellaro, P. Quantum sensing. *Rev. Mod. Phys.* **89**, 035002 (2017).
6. Gali, Á Ab initio theory of the nitrogen-vacancy center in diamond. *Nanophotonics* **8**, 1907 (2019).
7. Gali, Á Recent advances in the ab initio theory of solid-state defect qubits. *Nanophotonics* **12**, 359 (2023).
8. Huxter, V. M., Oliver, T. A. A., Budker, D. & Fleming, G. R. Vibrational and electronic dynamics of nitrogen–vacancy centres in diamond revealed by two-dimensional ultrafast spectroscopy. *Nat. Phys.* **9**, 744 (2013).
9. Ulbricht, R. et al. Jahn-Teller-induced femtosecond electronic depolarization dynamics of the nitrogen-vacancy defect in diamond. *Nat. Commun.* **7**, 13510 (2016).

10. Liu, A., Cundiff, S. T., Almeida, D. B. & Ulbricht, R. Spectral broadening and ultrafast dynamics of a nitrogen-vacancy center ensemble in diamond. *Mater. Quantum Technol.* **1**, 025002 (2021).
11. Ulbricht, R. & Loh, Z.-H. Excited-state lifetime of the NV^- infrared transition in diamond. *Phys. Rev. B* **98**, 094309 (2018).
12. Ulbricht, R., Dong, S., Gali, A., Meng, S. & Loh, Z.-H. Vibrational relaxation dynamics of the nitrogen-vacancy center in diamond. *Phys. Rev. B* **97**, 220302 (2018).
13. Carbery, W. P., Farfan, C. A., Ulbricht, R. & Turner, D. B. The phonon-modulated Jahn–Teller distortion of the nitrogen vacancy center in diamond. *Nat. Commun.* **15**, 8646 (2024).
14. Ichikawa, T. et al. Cooperative dynamic polaronic picture of diamond color centers. *Nat. Commun.* **15**, 7174 (2024).
15. Gali, A. Time-dependent density functional study on the excitation spectrum of point defects in semiconductors. *Phys. Status Solidi (b)* **248**, 1337 (2011).
16. Ma, Y., Rohlfing, M. & Gali, A. Excited states of the negatively charged nitrogen-vacancy color center in diamond. *Phys. Rev. B* **81**, 041204 (2010).
17. Thiering, G. & Gali, A. *AbInitio* magneto-optical spectrum of group-IV vacancy color centers in diamond. *Phys. Rev. X* **8**, 021063 (2018).
18. Onizhuk, M. & Galli, G. Colloquium: decoherence of solid-state spin qubits: A computational perspective. *Rev. Mod. Phys.* **97**, 021001 (2025).
19. Deák, P., Aradi, B., Frauenheim, T., Janzén, E. & Gali, A. Accurate defect levels obtained from the HSE06 range-separated hybrid functional. *Phys. Rev. B* **81**, 153203 (2010).
20. Gali, A., Simon, T. & Lowther, J. E. An ab initio study of local vibration modes of the nitrogen-vacancy center in diamond. *N. J. Phys.* **13**, 025016 (2011).
21. Thiering, G. & Gali, A. Ab initio calculation of spin-orbit coupling for an NV center in diamond exhibiting dynamic Jahn-Teller effect. *Phys. Rev. B* **96**, 081115 (2017).
22. Gali, A., Janzén, E., Deák, P., Kresse, G. & Kaxiras, E. Theory of Spin-Conserving Excitation of the $N - V^-$ Center in Diamond. *Phys. Rev. Lett.* **103**, 186404 (2009).
23. Ivády, V., Abrikosov, I. A. & Gali, A. First principles calculation of spin-related quantities for point defect qubit research. *npj Comput. Mater.* **4**, 76 (2018).
24. Wirtitsch, D. et al. Exploiting ionization dynamics in the nitrogen vacancy center for rapid, high-contrast spin, and charge state initialization. *Phys. Rev. Res.* **5**, 013014 (2023).
25. Kollarics, S. et al. Terahertz emission from diamond nitrogen-vacancy centers. *Sci. Adv.* **10**, eadn0616 (2024).
26. Lian, C., Guan, M., Hu, S., Zhang, J. & Meng, S. Photoexcitation in solids: first-principles quantum simulations by real-time TDDFT. *Adv. Theory Simul.* **1**, 1800055 (2018).
27. Lian, C., Hu, S.-Q., Guan, M.-X. & Meng, S. Momentum-resolved TDDFT algorithm in atomic basis for real time tracking of electronic excitation. *J. Chem. Phys.* **149**, 154104 (2018).
28. Lian, C., Zhang, S.-J., Hu, S.-Q., Guan, M.-X. & Meng, S. Ultrafast charge ordering by self-amplified exciton–phonon dynamics in TiSe2. *Nat. Commun.* **11**, 43 (2020).
29. Runge, E. & Gross, E. K. U. Density-functional theory for time-dependent systems. *Phys. Rev. Lett.* **52**, 997 (1984).
30. Yabana, K. & Bertsch, G. F. Time-dependent local-density approximation in real time. *Phys. Rev. B* **54**, 4484 (1996).
31. Krieger, K., Dewhurst, J. K., Elliott, P., Sharma, S. & Gross, E. K. U. Laser-induced demagnetization at ultrashort time scales: predictions of TDDFT. *J. Chem. Theory Comput.* **11**, 4870 (2015).
32. Yabana, K., Sugiyama, T., Shinohara, Y., Otobe, T. & Bertsch, G. F. Time-dependent density functional theory for strong electromagnetic fields in crystalline solids. *Phys. Rev. B* **85**, 045134 (2012).
33. Doherty, M. W., Manson, N. B., Delaney, P. & Hollenberg, L. C. L. The negatively charged nitrogen-vacancy centre in diamond: The electronic solution. *N. J. Phys.* **13**, 025019 (2011).
34. Maze, J. R. et al. Properties of nitrogen-vacancy centers in diamond: The group theoretic approach. *N. J. Phys.* **13**, 025025 (2011).
35. Abtew, T. A. et al. Dynamic Jahn-Teller effect in the NV^- center in diamond. *Phys. Rev. Lett.* **107**, 146403 (2011).
36. Burian, M. et al. Structural involvement in the melting of the charge density wave in 1T-$TiSe_2$. *Phys. Rev. Res.* **3**, 013128 (2021).
37. Wang, S.-F., Hsu, Y.-F., Pu, J.-C., Sung, J. C. & Hwa, L. G. Determination of acoustic wave velocities and elastic properties for diamond and other hard materials. *Mater. Chem. Phys.* **85**, 432 (2004).
38. Meng, S. & Kaxiras, E. Real-time, local basis-set implementation of time-dependent density functional theory for excited state dynamics simulations. *J. Chem. Phys.* **129**, 054110 (2008).
39. Wang, Z., Li, S.-S. & Wang, L.-W. Efficient real-time time-dependent density functional theory method and its application to a collision of an ion with a 2D material. *Phys. Rev. Lett.* **114**, 063004 (2015).
40. Giannozzi, P. et al. QUANTUM ESPRESSO: a modular and open-source software project for quantum simulations of materials. *J. Phys. Condens. Matter* **21**, 395502 (2009).
41. Giannozzi, P. et al. Advanced capabilities for materials modelling with Quantum ESPRESSO. *J. Phys. Condens. Matter* **29**, 465901 (2017).
42. Perdew, J. P., Burke, K. & Ernzerhof, M. Generalized gradient approximation made simple. *Phys. Rev. Lett.* **77**, 3865 (1996).
43. Hamann, D. R. Optimized norm-conserving Vanderbilt pseudopotentials. *Phys. Rev. B* **88**, 085117 (2013).
44. van Setten, M. et al. The PseudoDojo: training and grading a 85 element optimized norm-conserving pseudopotential table. *Comput. Phys. Commun.* **226**, 39 (2018).
45. Monkhorst, H. J. & Pack, J. D. Special points for Brillouin-zone integrations. *Phys. Rev. B* **13**, 5188 (1976).
46. Popescu, V. & Zunger, A. Extracting E versus k effective band structure from supercell calculations on alloys and impurities. *Phys. Rev. B* **85**, 085201 (2012).
47. Lian, C. & Meng, S. Dirac cone pairs in silicene induced by interface Si-Ag hybridization: a first-principles effective band study. *Phys. Rev. B* **95**, 245409 (2017).
48. Pacilè, D. et al. Narrowing of D bands of FeCo layers intercalated under graphene. *Appl. Phys. Lett.* **118**, 121602 (2021).
49. Momma, K. & Izumi, F. *VESTA 3* for three-dimensional visualization of crystal, volumetric and morphology data. *J. Appl. Crystallogr.* **44**, 1272 (2011).
50. Jin, Y., Yu, V. W.-Z., Govoni, M., Xu, A. C. & Galli, G. Excited state properties of point defects in semiconductors and insulators investigated with time-dependent density functional theory. *J. Chem. Theory Comput.* **19**, 8689 (2023).
51. Lian, C. Ultrafast laser induces macroscopic symmetry-breaking of diamond color centers. *Code Ocean* https://doi.org/10.24433/CO.3328944.V1 (2026).

Acknowledgements

C.L. thanks Ádám Gali for the helpful discussion. We acknowledge the financial supports from National Key Research and Development Program of China, Grant No. 2024YFA1408603 and CAS Project for Young Scientists in Basic Research under grant No. YSBR-120. Computational resources were provided by Xi'an Buhan and China HPC Platform.

Author contributions

C.L. proposed the study, supervised and obtained funding to support the project. Y.G. and C.L. performed the calculations and data analysis. Y.G. and C.L. drafted the initial paper, and all authors contributed to the writing of the manuscript.

Competing interests
The authors declare no competing interests.

Additional information
Supplementary information The online version contains supplementary material available at https://doi.org/10.1038/s41467-026-72813-x.

Correspondence and requests for materials should be addressed to Chao Lian.

Peer review information *Nature Communications* thanks Gergo Thiering and the other anonymous reviewer(s) for their contribution to the peer review of this work. A peer review file is available.